PHYSICAL REVIEW RESEARCH **8**, 033142 (2026)

Low-quality nonlinear resonators for phase thresholders and their applications in optical computing

Ivan A. Pshenichnyuk,[*] Kamil R. Taziev, Sergey S. Kosolobov, and Vladimir P. Drachev
Skolkovo Institute of Science and Technology, Moscow 121205, Russian Federation

(Received 26 June 2024; accepted 20 July 2026; published 5 August 2026)

Nonlinear integrated optical devices that can realize threshold filtration of signals are in demand in photonics and optical computing. However, a list of requirements exists for such devices to make them practical. Here, to design a thresholder with the desired behavior, we suggest a mechanism that implements the property of resonators to provide extremely sharp (with respect to the wavelength) π phase shifts near the critical coupling regime. By combining this feature with a nonlinear switching mechanism, one may obtain highly sensitive devices. Notably, the sharpness of the phase step in the considered case is independent of the quality factor of the resonators and the corresponding width of the resonances in transmittance. Instead, it is defined by the proximity to the critical coupling regime. Balancing near the critical coupling allows one to vary the sensitivity and achieve controllable smearing of the step function. The described effect is quite robust and can be realized for different materials and types of nonlinearity. The possibility of using sharp steps and low-quality resonators simultaneously provides multiple advantages for the resulting device. These include compact size, low manufacturing requirements, high operation speed, and low switching intensities. These sensitive and tunable phase thresholders may have multiple applications in optical computing. Few examples are provided, including a minimally invasive logic gate and a signal intensity classifier. In particular, the considered thresholders are useful in neuromorphic chips since they may act as optical neurons. In this paper, we provide an example of a photonic scheme that represents the behavior of a neuron and discuss its characteristics. Both the amplitude and phase of light are actively used in the scheme to store and update the state of a neuron.

DOI: 10.1103/x6vm-d1n3

I. INTRODUCTION

Optical microresonators play a significant role in integrated photonics. Silicon waveguides evanescently coupled to ring or disk resonators have numerous applications in photonic circuits [1–3]. One of the most obvious examples is a resonator-based filter. At certain resonant wavelengths, destructive interference between multiple waves passing various ways in a resonator cavity, causes the absence of transmittance at the output of the coupled waveguide, similar to Fabry-Perot etalon [4]. Filtering effects become particularly interesting when nonlinearity in the ring is involved. The dependence of transmittance on the intensity of a passing wave in the vicinity of a resonance may be quite peculiar [5–7]. Nontrivial shapes can be used to create photonic nonlinear elements, such as thresholders and logic gates [8,9]. It has also been suggested for use in neuromorphic photonic chips [10–12].

Particularly important for applications in the field of photonic artificial intelligence are elements that can realize the activation function (or logistic function) [13–15]. They are used to check if a signal collected by a neuron is above or below a certain threshold. There exists a list of requirements for such an element to make it practical. To allow neuromorphic algorithms, such as the Ising machines [16,17], to solve a general class of problems, the value of a threshold must be dynamically tunable. This becomes especially important in optimization problems, where each photonic neuron should have its own threshold. Moreover, there must be a possibility to switch between sharp and smooth step functions, with a well-controlled degree of smearing. It is used to switch between deterministic and stochastic regimes and vary the degree of chaos in the system. In a mathematical sense, the perfect shape for an activation function is provided by the Fermi-Dirac distribution with a variable "chemical potential" and "temperature" [13]. From this point of view, the curves provided by the intensity-dependent transmittance of nonlinear resonators are not sufficiently good [10].

In search of an appropriate optical signal transformation mechanism, the phase variation in resonator-based filters deserves particular attention. The phase shift is quite strong in the vicinity of a resonance. Thus, a nonlinear variation in a resonant condition may cause intensity-dependent switching that generates the required activation curve with the desired properties [18]. Different variations of this effect have been proposed to develop active nonlinear devices [19]. Phase switching can be easily transformed into amplitude switching via interference effects. The possibility of using phase and interference in optical computing makes it qualitatively different from electronics.

An important characteristic of resonators is the width of the resonances, which is directly linked with their quality

[*]Contact author: i.pshenichnyuk@skoltech.ru

factors and losses. In general, a large width makes the nonlinear switching mechanism problematic. A significant intensity must be applied to modify the resonant condition strongly enough to provide shifting from one side of the resonance to another. This statement is valid for both amplitude and phase switching. A large switching intensity is impractical from the point of view of the industrialization and stability of devices. To decrease the switching intensity, materials with strong nonlinear properties can be used [20]. Unfortunately, classical materials used in photonic chip building are not among them. Increasing the quality of resonators may decrease the impact of both of the abovementioned factors, but the production of such resonators can be challenging.

The phase shifting behavior of ring resonators becomes special close to the critical coupling regime [21–23]. Instead of a 2π phase shift smeared over the resonance, one obtains a sharp π shift in the middle of the resonance. Exactly in the critical coupling regime, we expect to obtain a perfect step function that can be broadened via small deviations from the regime. This broadening is quite thin and has nothing to do with the thickness of the resonances and their quality factor. A small thickness allows the system to be switched using materials with weak nonlinearities at relatively small intensities. From the point of view of applications, sharp phase steps allow the construction of nonlinear active devices with extremely large (and tunable) sensitivity.

In this work, we suggest combining sharp phase steps in nearly critically coupled resonators with a nonlinear switching mechanism for the realization of a sensitive phase thresholder, which can be applied in optical computing and, in particular, neuromorphic photonics. In Sec. II, we present the set of models that demonstrate the essence of the effect and allow us to evaluate its characteristics. Both analytical and numerical models based on nonlinear Maxwell equations are implemented. The results demonstrate that the effect is quite robust and universal. This can be achieved in low-quality resonators made from different materials with various types of nonlinearities. This approach brings us to the concept of a phase thresholder with many practical advantages, including a small size, fast operation speed, low manufacturing requirements, and low operational intensities of light. A few possible applications are discussed in Sec. III, including logic gates and condition checking. The most interesting possible application of the considered device is revealed in the field of neuromorphic photonics, where it perfectly reproduces the activation function in phase space with a tunable degree of smearing. The scheme of a neuron based on the suggested thresholder is demonstrated. For the first time, to the best of our knowledge, both the phase and amplitude of light are simultaneously utilized in one scheme to store the neuron state and reproduce its behavior. The suggested neuron can be a part of larger schemes, such as Ising machines. In Sec. IV, we discuss an efficient mechanism of electro-optical tuning that can be used to control the degree of smearing of the step function and vary the resonator parameters in the vicinity of the critical coupling regime. Thin indium-tin-oxide (ITO) layers deposited on the top of the resonator are used to achieve this. The results of computationally heavy three-dimensional (3D) modeling are presented and discussed. The paper is then concluded in Sec. V. In addition, we provide two Appendixes. In Appendix A, we discuss the theoretical low-quality limit, or, in other words, how bad the resonator can be to demonstrate extremely sharp phase steps discussed in the paper. In Appendix B, we provide the results of time domain analysis to demonstrate how noise of different types and amplitudes may influence the width and shape of a perfect theoretical step function. The time-domain Lugiato-Lefever equation (LLE) is solved numerically to achieve this.

II. FORMULATION OF THE CONCEPT AND COMPUTATION RESULTS

The straight-through transmission coefficient S of a ring resonator-based filter with one coupled waveguide can be expressed in the following form [4]:

$$S = \frac{ae^{i\varphi} + ib}{1 - iabe^{i\varphi}}. \tag{1}$$

It links the input and output complex wave amplitudes as $A_{\rm out} = SA_{\rm in}$. Here, $\varphi = 2\pi L n_{\rm eff}/\lambda$ is a phase shift acquired by the wave after one full pass around the ring, L is the length of the resonator, $n_{\rm eff}$ is the effective index of a waveguide mode, and λ is the wavelength. The amplitude attenuation coefficient a varies between 0 and 1 and defines losses in the ring (1 corresponds to a lossless ring), whereas $b = \sqrt{\eta}$ defines the coupling strength between the waveguide and the ring. The splitting ratio η is defined as the fraction of power that travels straight through the coupler. Thus, $(1 - \eta)$ is a fraction coupled to the ring. By computing the absolute square of Eq. (1), one can obtain the well-known formula for the transmittance of a ring resonator-based filter [4]. Correspondingly, a complex argument of Eq. (1) yields the phase shift. The critical coupling condition in our notations is written as $a = b$. It is easy to check that the in-resonance transmittance becomes strictly zero in this case.

In Fig. 1, three types of phase behavior near a resonance are demonstrated. Here, the ring with a radius $R = 10$ μm ($L = 2\pi R$) is considered with the effective index of the mode $n_{\rm eff} = 2.4$. This is a typical value for a TE mode of a silicon waveguide ($n_{\rm Si} = 3.48$) with a cross section of 500 nm × 220 nm, assuming that the claddings are made from SiO_2. Exactly in the critical coupling regime (red curve), when losses are balanced with coupling, there is one sharp π phase shift in the center of the resonance. It can be made smoother in the undercoupled regime when $b > a$ (dashed blue curve). In contrast, in the overcoupled regime, when $a > b$, we obtain a smooth 2π phase shift (dash-dotted green curve). In the latter case, the variation in phase takes place in the range of wavelengths that coincides with the width of the resonance. In the other two cases, the thickness of the sharp π phase shift is defined by the proximity to the critical coupling regime and does not depend on the width of the resonance or its quality factor.

In general, the quality factor of a resonator is expressed as the frequency of a resonance divided by its full width at half maximum (expressed in hertz). In our analytical model, it is predefined by parameters a and b. For example, for $a^2 = b^2 = 0.5$, the quality factor is 472, which is rather low and is characterized by broad resonances in the spectrum. Taking another set of parameters, for example, $a^2 = b^2 = 0.9$ (used

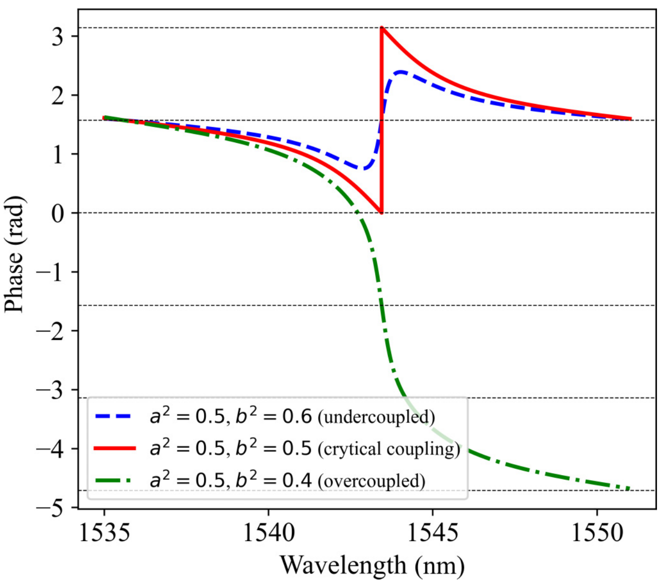

FIG. 1. Three types of phase variation occurring in ring-based filters near a resonant wavelength. The linear model is based on Eq. (1) and the plotted quantity is Arg(S). The coupling and loss parameters are shown in the legend. The curves are presented for a ring resonator with $R = 10$ μm and $n_{\mathrm{eff}} = 2.4$. The quality factors Q for the critically coupled, overcoupled, and undercoupled resonators are 472, 421, and 540, respectively.

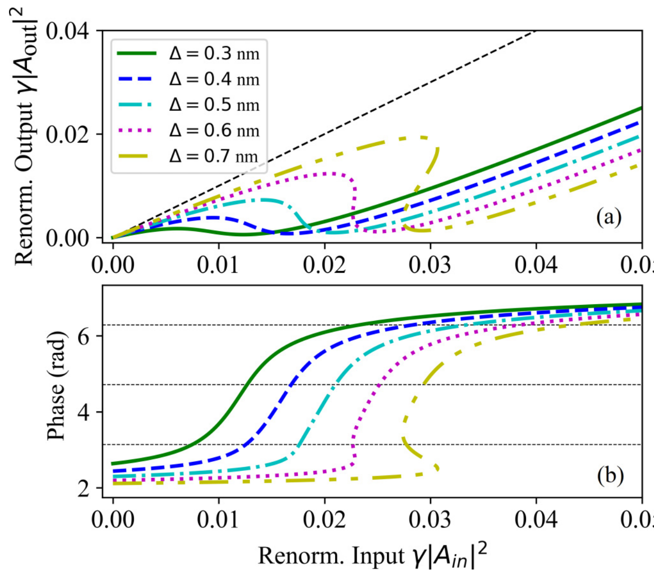

FIG. 2. Dependence of the output intensity [panel (a)] and phase [panel (b)] on the input intensity in nonlinear ring resonators. The intensities are renormalized to make the result universal and independent of the specific value of γ (see the text). Different values of the detuning Δ are shown (see the legend). The nonlinear model is based on Eqs. (3) and (4). The results are shown for the overcoupled resonator with $a^2 = 0.9$, $b^2 = 0.85$, and $Q = 2301$. The geometry of the ring coincides with the resonator presented in Fig. 1.

in Fig. 3), we can slightly increase the quality up to 2943, but it is still considered low compared with modern experimental achievements [24].

In a nonlinear resonator, the refractive index of its material depends on the signal amplitude, which we denote as A_r. This fact results in an additional amplitude-dependent phase shift in the ring. For the minimalistic practical theory of nonlinear resonators, it is sufficient to assume quadratic dependence,

$$\varphi(|A_r|^2) = \frac{2\pi L}{\lambda} n_{\mathrm{eff}} + \gamma |A_r|^2, \tag{2}$$

with a nonlinear coefficient γ. If one explicitly refers to Kerr nonlinearity in the ring, the coefficient γ can be linked with the corresponding n_2 coefficient. In the results presented here, we do not assign a specific number for γ but use relative units instead (see below).

It becomes challenging to obtain an analytical expression for the straight-through transmission coefficient S in the nonlinear case since the phase depends on A_r. Nevertheless, it is possible to write the solution in the parametric form

$$A_{\mathrm{in}} = A_r \frac{1 - iabe^{i\varphi(|A_r|^2)}}{\sqrt{1-b^2}}, \tag{3}$$

$$A_{\mathrm{out}} = A_r \frac{ae^{i\varphi(|A_r|^2)} + ib}{\sqrt{1-b^2}}. \tag{4}$$

Allowing A_r to pass a certain range of values, one obtains numerically both A_{in} and A_{out} and thus can reconstruct the coefficient S. Since A_r in Eqs. (3) and (4) stands under the argument of a periodic function, in certain cases, multiple combinations exist that correspond to bistable regimes of the resonator [5,25,26].

In Fig. 2, we show the dependence of the phase and renormalized output intensity on the input intensity for a nonlinear ring-based filter. To keep the analysis general, we express the intensities in units of $\gamma|A|^2$. The structure of Eqs. (3)

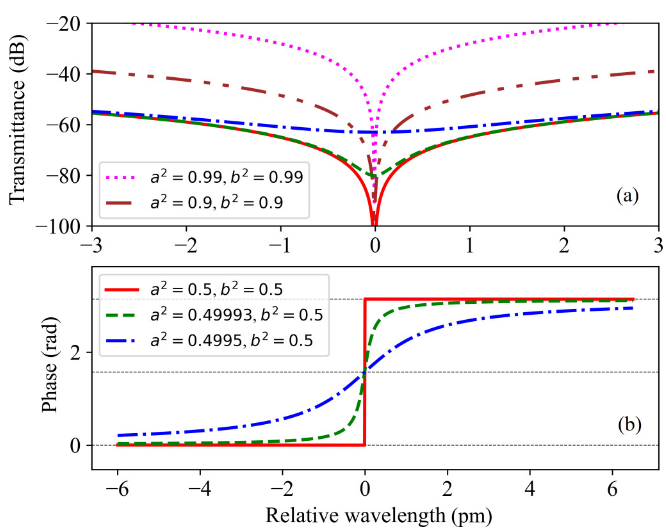

FIG. 3. Transmittance [panel (a)] and phase [panel (b)] at the output of the resonator plotted as a function of the relative wavelength close to the critical coupling regime. The linear equation (1) is used. The geometry of the ring resonator concides with those of the previous examples (Figs. 1 and 2). The quality factors for the critically coupled regimes denoted by the solid red line, dash-dot-dotted brown line, and dotted magenta line are 472, 2943, and 30 394, respectively.

and (4) allows to multiply both sides by $\sqrt{\gamma}$ and rescale the amplitudes as $\sqrt{\gamma}A_{\text{in}} = A'_{\text{in}}$, $\sqrt{\gamma}A_{\text{out}} = A'_{\text{out}}$, and $\sqrt{\gamma}A_r = A'_r$. This allows the comparison of different phase switching mechanisms without considering the details of the specific nonlinear mechanism involved. Below, we also provide the numerical simulation results with an absolute intensity scale for Kerr nonlinearity in silicon. The wavelength in Fig. 2 is slightly shifted with respect to the resonance. Different values of the detuning Δ are considered (see the legend). Detuning enters Eq. (2) through the wavelength $\lambda = \lambda_0 + \Delta$, where λ_0 is the resonant wavelength. The black dashed line denotes the $|A_{\text{in}}|^2 = |A_{\text{out}}|^2$ condition, which one would expect to observe in the linear out-of-resonance regime. Thus, it defines the asymptotic behavior at small intensities. By increasing the input intensity, we force the system to pass through the resonance. The intensity decreases and then increases; at the same time, phase switching occurs. Notably, detuning Δ should be positive. Otherwise, if the displaced wavelength is located at a lower value than the center of the resonance, the described mechanism does not generate a step, since the shift caused by the intensity [Eq. (2)] is unidirectional. For greater detuning, the threshold intensity also increases. A high intensity, in turn, initiates bistable regimes (dotted magenta and dash-dot-dotted yellow curves). This phenomenon is well known in the theory of nonlinear resonators of different types [27]. There are examples in the literature that demonstrate how bistability may turn into multistability in some regimes with even more complicated forms of curves [28]. Various multistable regimes also appear in systems containing multiple coupled resonators. A bifurcation diagram in this case becomes complicated and contains multiple areas, including stable, unstable, multistable, and self-pulsing regimes. Multiple applications of such systems in integrated photonics are possible [29,30]. The phase profiles shown in Fig. 2(b) are, in principle, suitable for representing the activation function. However, to obtain very sharp steps, extremely high-quality resonators are needed. Moreover, dynamic control of sharpness can also be problematic in this case. It is also necessary to stress that for applications that we have in mind (Sec. III), bistability is a rather undesired effect, which we would try to avoid. Otherwise, the form of the curves, especially for phases [Fig. 2(b)], becomes too complicated to represent a well-behaved thresholder. At the same time, other approaches exist, where bistability is required [10]. The prevention of bistability in our case means that we have to keep the intensity low, avoiding multiple solutions of Eqs. (3) and (4). As will be demonstrated below, this is perfectly allowed by our approach.

Now, we discuss an alternative switching scheme in the vicinity of the critical coupling regime. We use the solid red and dashed blue curves instead of the dash-dotted green curve in Fig. 1. The dependence of the transmittance and phase in these regimes on the wavelength is shown in Fig. 3. Since the plotted feature is rather thin, a relative with respect to the position of the resonance wavelength scale is used. The width, which is just a few picometers in size, allows the use of small values of detuning and requires much smaller intensities for switching (discussed below).

The solid red, dashed green, and dash-dotted blue curves in Fig. 3 correspond to the lowest-quality resonator with slightly varied losses. When one increases losses (by decreasing a), a perfectly sharp step function becomes a smoothed Fermi-Dirac-like shape, providing exactly the type of behavior we are looking for. Such a modification of losses can be achieved, for example, by integrating an absorption modulator into the ring [31–34]. For comparison, two more critically coupled resonators with higher quality factors (dash-dot-dotted brown and dotted magenta curves) are considered. They both provide perfect step functions with respect to a phase that are indistinguishable from the solid red curve in Fig. 3(b). The difference occurs in the transmittance [Fig. 3(a)]. Since the effect is observed close to the resonance, the transmittance is generally low, and we use a logarithmic scale. In the center of the resonance, where $T = 0$, the curve goes to $-\infty$ in the critical coupling regime but grows when the losses are increased (dashed green and dash-dotted blue lines). In general, higher-quality resonances provide greater transmittance. However, the quality has no influence on the curvature of the phase step. Low transmittance also takes place for the thresholders depicted in Fig. 2. For the switching mechanism based on critical coupling, it is obviously lower but still quite measurable. Importantly, since the minima in transmittance are an interference effect, the energy is not lost and can be collected, for example, if we add the second waveguide to the ring (drop port, see below). This signal can be used elsewhere in the circuit. Thus, although the output transmittance is low, the overall losses in such a device can be minimal.

The phase steps produced by nonlinear resonators with a variable input intensity in the vicinity of the critical coupling regime are shown in Fig. 4. The results extracted from the analytical computations [Eqs. (3) and (4)] are shown in Fig. 4(a). As expected, a sharp step is observed in the critical coupling regime, and it can be smeared by increasing losses in the ring. The detuning is set to $\Delta = 6$ pm. In this case, the phase step appears at a relative intensity close to 0.0012 [Fig. 4(a), solid red line]. This value is almost 20 times smaller than the position of the steps in Fig. 2(b), which is on the order of 0.02. Thus, the switching in Fig. 4(a) takes place at much smaller intensities, away from the bistable regimes. For the comparison, one additional curve is added with a slightly increased quality factor [yellow dotted curve in Fig. 4(a)]. The sharpness of the step is exactly the same, but it appears at an even smaller intensity. The explanation is that resonators with larger quality factors accumulate larger intensities inside at a fixed input intensity. This allows us to decrease the switching threshold even further. However, again, it has no influence on the quality of the thresholder. The desired π phase shift is clearly obtained for the proposed device. In contrast, in Fig. 2, the shift is larger than π. This is because the system only partially passes through the broad resonance in a given intensity range; otherwise, a 2π shift would be obtained (see the dash-dotted green curve in Fig. 1). To obtain an exact π shift (useful for applications) for the devices depicted in Fig. 2, the detuning and intensity have to be additionally calibrated.

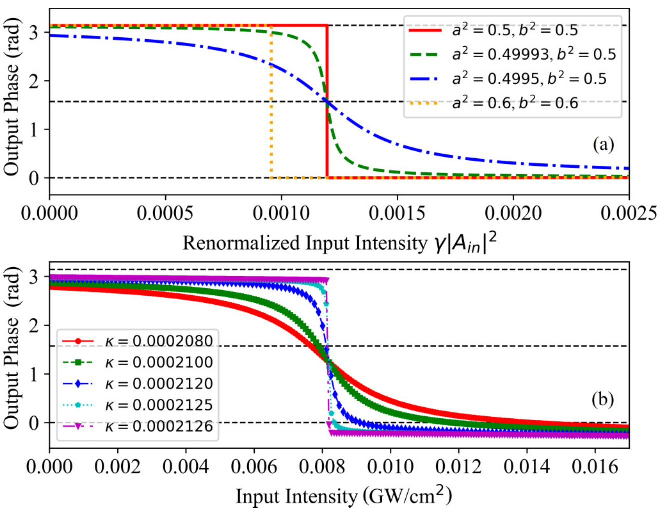

FIG. 4. (a) An output phase of a nonlinear resonator as a function of the renormalized input intensity obtained from the semianalytical model [Eqs. (3) and (4)]. The quality factors for the critically coupled regimes, i.e., the solid red curve and the dotted orange curve, are 472 and 627, respectively. A ring resonator with a geometry from the previous examples (Fig. 1) is used. The value of the detuning is fixed at $\Delta = 6$ pm. (b) Numerical results obtained from the Maxwell simulations for a resonator with a variable loss coefficient κ. The following parameters are used: ring radius $R = 5$ μm, waveguide width $w = 220$ nm, gap width $g = 239$ nm, Kerr coefficient for Si $n_2 = 6 \times 10^{-5}$ cm^2/GW, and detuning $\Delta = 10$ pm. The obtained quality factor is $Q = 4118$. Thus, different computational approaches applied to resonators with different parameters allow the discussed regime with a sharp π phase jump to be found, assuming that the parameters are carefully chosen.

Summarizing the results obtained up to this point, we may conclude that, to switch from the broad, partially bistable 2π step functions in Fig. 2(b) to perfectly sharp π steps in Fig. 4(a), it is crucial to set parameters close to the critical coupling regime (red solid curve in Fig. 1) and pick the right values for detuning and intensity. The described analytical approach significantly simplifies the search for corresponding steps during nonlinear numerical modeling (see below). The physical mechanism behind the appearance of the sharp phase step can be revealed by analyzing the output of the resonator, which is represented as a result of multiwave interference. This is discussed in more detail in Appendix A.

In Fig. 4(b), we present the results of the numerical simulations. The frequency-domain Maxwell equations in the form of second-order wave equation for the electric field were solved. Kerr nonlinearity is added through the refractive index of silicon, which locally depends on intensity. The numerical solver that utilizes the finite element method is realized in COMSOL Multiphysics 5.3a. Please find the details of the approach in our previous works [20,31]. The set of parameters required to reproduce the calculations includes the geometry and refractive indices of the materials. The numbers are provided below. As predicted by our model, the thresholding behavior is universal and is defined mainly by the proximity to the critical coupling regime. This is illustrated by the significant variation in the geometry in the numerical simulation. In the next section, we consider even more radical variation. Nonlinear Maxwell equations were solved for a ring resonator with a radius of 5 μm and a waveguide width of 220 nm. Its actual quality factor is close to 4118. The value of the detuning $\Delta = 10$ pm is used in the simulations. Parameters a and b cannot be directly incorporated into the numerical model. The losses are controlled through the imaginary part κ of the refractive index $n = n' + i\kappa$, which enters the Maxwell equations [shown using different linestyles in Fig. 4(b)]. The coupling depends on the distance between the waveguide and the ring, which is equal to 239 nm in the simulation. We also explicitly incorporate the Kerr coefficient for silicon, $n_2 = 6 \times 10^{-5}$ cm^2/GW.

The numerical model is quite different from the analytical model for many reasons. For example, the correct dependence of the effective index on the wavelength is taken into account. The coupler is an extensive structure instead of the "point coupler" considered in analytical computations. Nonlinearity takes place not only in the ring but also in the straight part of the waveguide. Certain coupler losses occur in the numerical model, in contrast with the idealized lossless coupler considered previously. We do not model explicitly possible manufacturing imperfections and consider their influence to be negligible at the length scale of the device. Despite the multiple differences between the analytical and numerical models, the threshold behavior in both models is quite similar. In the numerical model, an absolute intensity scale linked directly with the Kerr nonlinearity of silicon is obtained. Typically, to observe this type of nonlinearity in silicon, much larger intensities should be applied, which are achievable only for pulsed lasers. In our example, the threshold intensity is rather small (0.008 GW/cm^2, instead of the few GW/cm^2 typically used in this context [5]). Thus, the suggested mechanism may be practically applicable even for continuous lasers. Kerr nonlinearity in silicon is also quite fast, and its usage has many advantages for applications.

Many nonlinear effects are known to exist in silicon. In addition to the Kerr effect, the list includes thermal nonlinearity, free-carrier effects, and two-photon absorption [1,35]. Other nonlinearities have also been suggested for use in the context of thresholders [12,36]. The Kerr nonlinearity, used in the numerical simulation above, is the fastest. Its response time is on the order of subpicoseconds. At the same time, free-carrier based effects are restricted by the lifetime of the carriers. In silicon, it is typically on the order of a few hundreds of picoseconds. The thermal response time is on the order of microseconds. Even though Kerr nonlinearity can be weaker in Si, compared with other nonlinear mechanisms (depending on the wavelength range), it can still be separated [37,38]. We also note that the discussion in the first part of our paper is quite general. This means that different nonlinear mechanisms can be used to perform phase switching in low-quality resonators. Moreover, very similar results can be obtained for resonators made from alternative materials, such as Si_3N_4.

The speed of operation in resonator-based devices depends not only on a typical timescale of nonlinearity but also on the "charging time" of a resonator. This is the point where our approach has significant advantages over high-quality resonators. The typical charging time τ, associated with a resonator, is proportional to a quality factor Q. Up to this point,

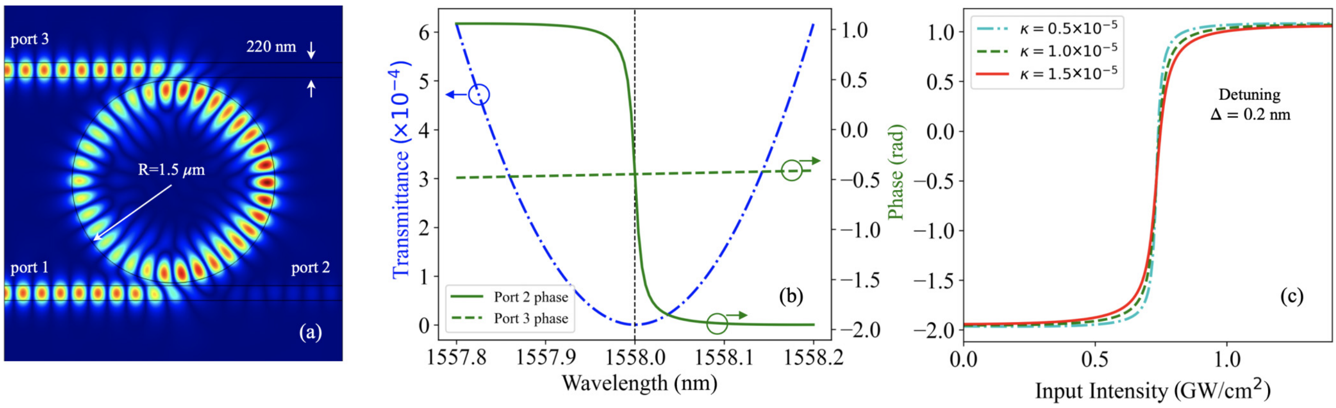

FIG. 5. The results of numerical Maxwell simulations demonstrate the use of the discussed principles for realizing a low-loss thresholder via an extremely simple and compact low-quality disk resonator with two attached waveguides. The figure shows (a) the geometry and electric field distribution inside the device, (b) the behavior of the transmittance and phase in the two output ports of the device as a function of the wavelength, and (c) the nonlinear threshold switching achieved in the device via a small variation in the intensity and corresponding value of detuning. The main parameters required to reproduce the calculation are shown in the figure. The gap widths are set to 50 nm each. The resulting quality factor is $Q \sim 96$.

we consider quality factors of approximately 500 (in some examples, up to a few thousand). Below, we demonstrate a working model with a quality around 100. The telecom wavelengths of approximately 1.55 μm correspond to the typical times τ on the order of picoseconds. This time perfectly correlates with the subpicosecond timescale of Kerr nonlinearity. Theoretically, this promises devices that operate at terahertz frequencies. This is significantly larger than, for example, the numbers reported in Ref. [8] for Mach-Zehnder interferometer (MZI) based thresholders, where the operation frequencies are in the gigahertz range. The time-domain phenomena related to our models are discussed in more detail in Appendix B. Another advantage of low-quality resonators is that they accumulate much less power (the intensity enhancement factor is proportional to the quality factor). The low intensity stored inside the device allows the avoidance of undesired heating effects.

To demonstrate how the ideas discussed above can be developed further, we present a model of a three-terminal nonlinear thresholder, which is formed by a resonator symmetrically coupled with two 220 nm wide identical waveguides. To demonstrate the universality of the effect, the disk resonator, which supports whispering gallery modes, is considered instead of a ring resonator [see Fig. 5(a)]. The disk radius is just 1.5 μm, which makes the resulting device rather compact and simple to manufacture. The large curvature causes significant losses and, correspondingly, a small quality factor. The material loss of silicon enters the model through the imaginary part of its refractive index $\kappa = 10^{-5}$. This number can be varied in both directions passively, by doping, or through the implementation of one of the available active tuning mechanisms [20,31,33] (Sec. IV). The vicinity to the critical coupling regime is guaranteed by the optimized 50 nm gap between the disk and the waveguides. Numerical simulations are used to characterize the structure. The computational approach and equations are the same as those employed above to compute the curves in Fig. 4(b).

The considered device has a resonance at 1558 nm. As expected, close to the resonance at port 2 [shown in Fig. 5(a)], we observe a sharp and tunable π phase step accompanied by a low signal amplitude [see Fig. 5(b)]. In contrast with the previous demonstrations, the remaining energy travels to port 3. This makes the device almost lossless. Notably, the phase jump does not take place at port 3 [green dashed line in Fig. 5(b)]. The width of the considered resonance at the half maximum is close to 16 nm. According to the above definition, the quality factor is ~ 96, which is the lowest value considered in this paper thus far. At the same time, the width of the phase step is only ~ 0.1 nm, which is 2 orders of magnitude smaller [green solid line in Fig. 5(b)]. In the selected regime, the transmittance at the resonance minimum is -63 dB [blue solid line in Fig. 5(b)] and can be challenging to measure. At the same time, shifting the wavelength just for 0.08 nm allows us to obtain a value of -40 dB, which is easily measurable. The general idea is to keep this number as small as possible but measurable, balancing near the critical coupling regime. The transmittance increases rapidly when one moves away from the critical coupling. The price to pay for greater transmittance in this case is the phase step broadening and corresponding reduction in the sensitivity of a device. Thus, an appropriate balance should be found, depending on the application. Alternatively, in some cases, the switching can be organized such that the central part in a certain vicinity of the resonance is not used.

To reproduce an activation function, we introduce the detuning $\Delta = 0.2$ nm. In this case, by increasing the intensity, one may move through the phase step from the right-hand side [Fig. 5(b)] to the left. This generates the perfect tunable activation function, as demonstrated in Fig. 5(c). A slight modification of κ causes the desired smearing effect. From Figs. 5(b) and 5(c), we can conclude that the broadening of the step of approximately 0.05 nm in the "wavelength domain" causes broadening of approximately 0.25 GW/cm^2 in the "intensity domain." Thus, the possible wavelength instability of a laser within 0.05 nm would not cause additional step broadening. The small width of the step allows us to observe the effect at relatively small intensities to compare with bistable regimes (Fig. 2). This, in turn, potentially allows

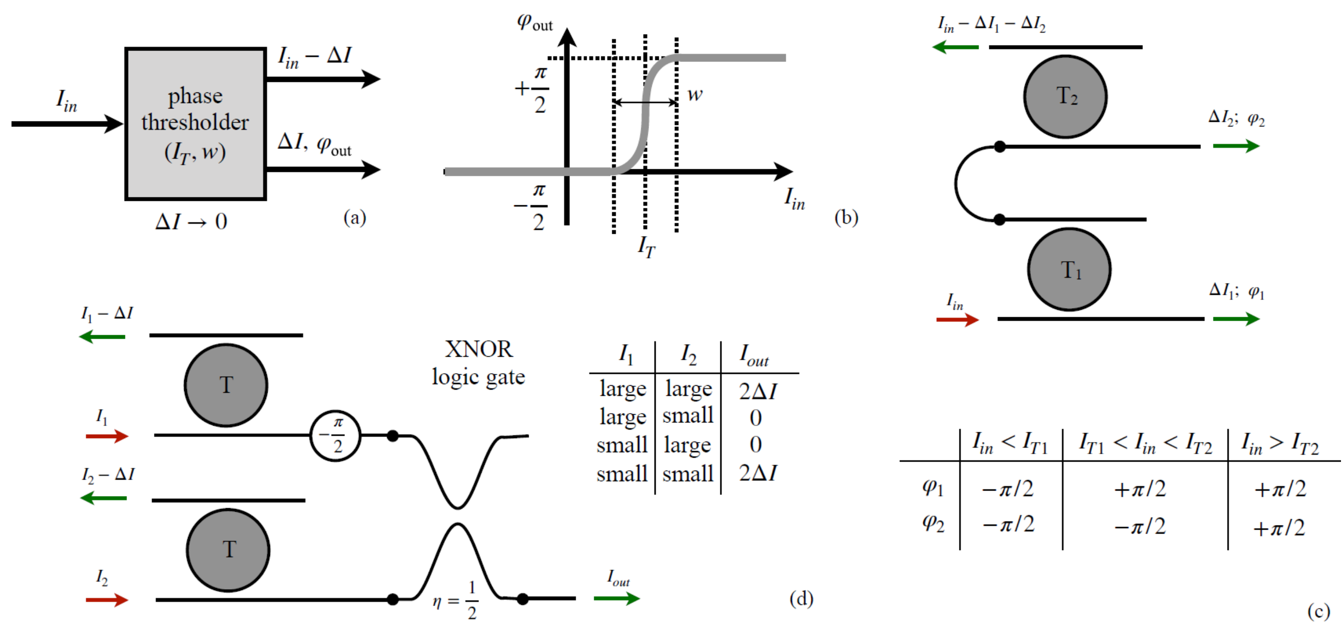

FIG. 6. Schematic illustration of the suggested thresholder functionality and possible applications: (a) the three-terminal thresholder scheme, (b) the phase output vs intensity input characteristics curve, (c) the scheme that can be used to classify the signal inside the waveguide with respect to three intensity intervals, and (d) the scheme of a minimally invasive xnor logic gate obtained from two thresholders and one directional coupler.

the application of the device in the continuous wave regime and the use of conventional materials. Additionally, supplementary layers of materials on top of the resonator, which are required for tuning [31], unavoidably decrease the quality of the resonator. From this point of view, the robustness of the effect with respect to the quality factor is a valuable property. Other types of integrated resonators can also be considered in the future to realize the studied mechanism, such as samples based on Bragg mirrors, photonic crystals, and inverse design structures [39,40].

III. APPLICATIONS

Summarizing the obtained results, we introduce a device that works as a minimally invasive phase thresholder with one input and two output channels [Fig. 6(a)]. The input channel receives the intensity I_{in}. Then, the small fraction of this signal ΔI (theoretically, it can be made as small as needed; in our example from the previous section, it is $\sim$0.01%) is split and sent to one of the outputs. It also carries the phase $+\pi/2$ or $-\pi/2$ depending on whether the input intensity I_{in} is above or below a certain tunable threshold I_T. The original signal, which is attenuated just slightly and otherwise unchanged, is transmitted to the other output channel.

The dependence of the output phase φ_{out} on the input intensity I_{in} has the form of a step function [Fig. 6(b)]. The step width w and its position I_T are tunable quantities. The first can be varied via a small controllable source of losses incorporated into the resonator (see below). The step width w, depending on the desired application of the thresholder, theoretically can be made as small as required. The sharpness is defined by the proximity to the critical coupling regime. Theoretically, an infinitely sharp step is equivalent to an infinitely sensitive device. Importantly, high sensitivity (with respect to phase) can be reached for low-quality resonators (see also Appendix A). This useful property allows the realization of ultracompact resonators and the use of active electro-optical materials that introduce losses, such as doped silicon and ITO (see below).

There are multiple potential applications of the suggested device. Obviously, it can be used to check the level of signal propagating in a waveguide. For example, a scheme assembled from two thresholders [Fig. 6(c)] allows the assignment of the propagating signal to one of three possible intensity intervals. The interval is defined according to the phases detected at two control ports according to the table [Fig. 6(c)]. At the same time, the original signal that travels to the drop port of the second thresholder remains almost unchanged, been two times reduced by small values.

Another application example from the field of photonic computations is the optical xnor logic gate, which can be assembled from two thresholders, one passive phase shifter and one directional coupler [Fig. 6(d)]. To model the latter two elements, we employ the transmission matrix [4]

$$S_{\text{dc}} = \begin{pmatrix} \sqrt{\eta} & i\sqrt{1-\eta} \\ i\sqrt{1-\eta} & \sqrt{\eta} \end{pmatrix} \tag{5}$$

and transmission coefficient

$$S_{\text{ps}} = e^{i\phi} \tag{6}$$

for the directional coupler with splitting ratio η and the phase shifter with angle ϕ, respectively. In the considered gate [Fig. 6(d)], it is assumed that we address two possible discrete levels of intensity, which are conventionally large and small. Allowing two input signals I_1 and I_2 to pass through identical thresholders, one may separate large and small intensities. The evaluation results are encoded in phases. After

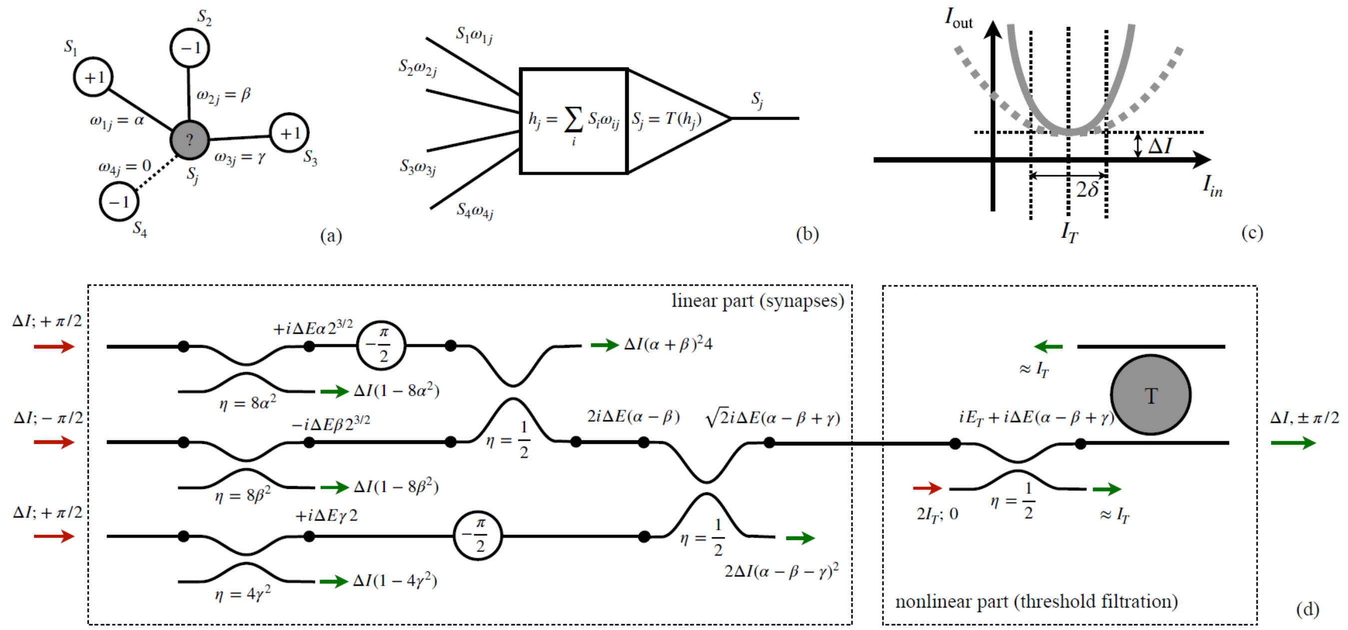

FIG. 7. Application of the phase thresholder as a nonlinear activation element in a neuromorphic photonic circuit: (a) simple network assembled from five neurons, (b) mathematical model of one single neuron behavior, (c) $I_{out}(I_{in})$ characteristics of the phase thresholder, and (d) example of a photonic circuit that mimics the behavior of a neuron.

that, we force the corresponding test signals to interfere, using the directional coupler with splitting ratio $\eta = 0.5$ and one passive phase shifter with $\phi = -\pi/2$. Since the thresholders return just two possible phase states, which differ by π, they interfere purely constructively or destructively. Evaluating the interference results intensity I_{out} depending on four possible combinations of input intensities I_1 and I_2, one obtains the truth table [Fig. 6(d)] that reproduces xnor logic. In addition, again, as in the previous example, the input energies that are only slightly reduced can be collected from the other two outputs and used elsewhere in the circuit.

In practice, the two thresholders in Fig. 6(d) can differ slightly because of manufacturing inaccuracies. Fine alignment near the critical coupling regime can be realized for each resonator via the mechanism described in Sec. IV to compensate for the difference. Input powers can also vary slightly. However, since the logic gate operates at two levels of a signal, we are free to choose them sufficiently far from the threshold power. The good choice would be to set them symmetrically at both sides of the threshold. In this case, owing to the form of the phase curve [Fig. 5(c)], small variations in the input powers would not influence the phase output of the thresholders. We also expect a certain intensity noise on top of the output power of thresholders ΔI. As long as it is reasonably smaller than ΔI itself, the interference in the directional coupler will reproduce the desired truth table [Fig. 6(d)]. It can be checked via Eqs. (5) and (6). The values of ΔI on the order of -40 dB discussed earlier in the text are well above the typical noise level in integrated photonics and allow us to realize the described mechanism. Moreover, the specific values of the allowed deviations depend on the application. A thorough noise analysis of the thresholders is presented in Appendix B.

The most interesting application perspective, from our point of view, is that the considered device may be used in the field of neuromorphic photonic circuits. The search for an optical thresholder that reproduces the functionality of neuron activation is an important problem in this field. Purely optical amplitude-based solutions exist (where electricity is used only to set the parameters of a device) [8] or mixed electro-optical realizations with signal transformations realized via photodetectors and electro-optical modulators [41,42]. The phase behavior of low-quality resonators near the critical coupling regime considered above is promising from this perspective. The possibility of implementing a purely optical solution where both the amplitude and phase of light are used is a natural advantage in the field of photonics. Let us quickly review here the functionality requirements for a neuron that may act as a part of the Ising machine, Boltzmann machine, or another neuromorphic algorithm. Afterward, we present and discuss an example of a photonic circuit that realizes the described functionality.

Let us consider a network of binary neurons $S_i = \pm 1$, where each element is connected with others according to the coupling matrix ω_{ij} [Fig. 7(a)]. At a certain moment, a neuron S_j receives a total signal from all other connected neurons, weighted by the coupling matrix and expressed as $h_j = \sum_i S_i\omega_{ij}$. Depending on whether h_j is above or below a certain threshold (in general, the threshold value is unique for each neuron), the state of the neuron S_j is defined as $+1$ or -1. This model is known as McCulloch-Pitts neuron [13] [Fig. 7(b)].

Notably, a family of algorithms exist where the state of neurons is considered continuous rather than binary [13]. It can potentially be useful for the realization of analog photonic brains. The first group of operations, related to the computation of h_j, mimics the functionality of synaptic connections in the human brain. It is realized via linear algebraic transformations. In certain algorithms (algorithms with synchronous updating [13]), h_j can be computed simultaneously for all neurons. In this case, it can be represented by matrix-vector multiplication. The second operation, namely, threshold filtration, defines the state of the neuron. It is by definition nonlinear.

For the demonstration below, the symmetric network is considered. In the coupling matrix, $\omega_{ij} = \omega_{ji}$, and the threshold is located at zero. The matrix ω_{ij} may contain both positive and negative elements, and it is also normalized, usually by the number of neurons. Thus, each element of the matrix is generally a small real number. This means that the total signal h_j received by the neuron lies within a certain small neighborhood of zero. These networks, also known as Hopfield networks, can be used for the storage and recognition of images [13]. Specifically, we assume that the considered neuron has nonlinear connections α, β, and γ with only three other neurons, $S_1 = +1$, $S_2 = -1$, and $S_3 = +1$, respectively [Fig. 7(a)].

The photonic circuit that realizes the required neuromorphic behavior is presented in Fig. 7(d). The information about the states of coupled neurons is used as input (three red arrows in the left part of the figure). The state of each neuron is encoded by phase $+\pi/2$ or $-\pi/2$. All the inputs have the same small but measurable intensity $\Delta I = |\Delta E|^2$. According to the analysis presented above, the expected values of ΔI are on the order of -40 dB. The intensity is given at all inputs and outputs of the scheme (red and green arrows, respectively). At the intermediate steps, we operate with the field amplitudes since the interference effects are important there.

It is well known in photonics that linear operations such as summation and multiplication can be realized via directional couplers. The possible linear part of the circuit, which includes five couplers and two phase shifters, is separated by the black dashed line on the left side of Fig. 7(d). The phase shifters in this scheme are passive. Their existence does not contribute much to the size of the circuit. Practically, the desired $-\pi/2$ shift can be obtained by increasing the length of the corresponding waveguides. We do not intend to provide an optimal scheme here. There are enough examples in the literature where for example, photonic processors are suggested to perform this operation simultaneously for each neuron via arrays of MZIs [43,44]. In this work, we concentrate on the nonlinear part, whereas the linear part is provided to make the discussion complete. The elements that enter the linear part of the circuit can be modeled via the coefficients defined in Eqs. (5) and (6). It is easy to check that at the output of the linear block, we have a field with an amplitude $i\sqrt{2\Delta I}(+\alpha - \beta + \gamma)$. Except for the phase factor, it is exactly the sum that represents the total signal h_j collected by the neuron. It can be both positive and negative. The provided scheme works for any combination of input states.

Now, we switch to the discussion of the nonlinear part [Fig. 7(d), second block]. Since our nonlinear resonator should have a threshold at a certain nonzero intensity $I_T = |E_T|^2$, the input signal should be shifted from the neighborhood of zero to the neighborhood of I_T. This can be realized via one more directional coupler, where an additional signal with an intensity of $2I_T$ is sent to the second input port of the coupler (red arrow) to interfere with the main signal. The intensity I_T does not have to be very large, but it should be much greater than ΔI. This is related to the fact that the output intensity of the thresholder (the signal that has $+\pi/2$ or $-\pi/2$ phases, not the drop port signal) is always a small fraction of the input intensity. According to the evaluations above, we assume that the ratio is on the order of -40 dB. Therefore, we want to make ΔI as small as the experiment allows, and correspondingly, I_T should be larger. Notably, I_T is still much smaller than that required for bistable switching, and the phase step is quite sharp (see, for example, Fig. 5). Another advantage of the presented nonlinear block is that it works as a local "amplifier," generating a signal with an intensity close to ΔI each time at the output. This prevents the signal degradation and enables convenient scaling. The unused energy can be collected from the drop ports.

The phase of the additional $2I_T$ signal in the nonlinear block should be orthogonal to both phases of the neural inputs ($+\pi/2$ and $-\pi/2$). It is easy to check via Eq. (5) that, in this case, the field amplitude at the input of the thresholder is $E_{\text{in}} = i\sqrt{I_T} + i\sqrt{\Delta I}(\alpha - \beta + \gamma)$. While the second term lies in the neighborhood of zero, the sum belongs to the neighborhood of E_T. Equivalently, the input intensity is $I_T \pm \delta$. In our example, $\delta \approx 2\sqrt{I_T \Delta I}(\alpha - \beta + \gamma)$ if we use the fact that $I_T \gg \Delta I$. Neglecting the terms of higher orders in ΔI, we may say that the intensity $2I_T$ that is used for condition checking can be collected almost unchanged from two output ports [green arrows inside the nonlinear block of Fig. 7(d)]. This signal can be used to perform threshold filtration of other neurons elsewhere in the circuit. Another obvious advantage of this approach is that the main part of the scheme operates at low intensity, whereas the large-intensity subcircuit is used only for condition checking. After the thresholder performs its operation, the small-amplitude signal with phases $+\pi/2$ or $-\pi/2$ that reflects the updated state of the neuron can be collected at the output port.

The intensity level at the output of the optical neuron deserves separate discussion. As mentioned earlier, we choose the value of ΔI to be as small as possible but measurable. The signals on the order of -40 dB considered above are sufficiently strong to be measured. For example, if we use a 0.4 W laser for condition checking, the output power is 0.04 mW. Additional postprocessing is required to measure the phase of a low-intensity signal since it encodes the neuron state in the suggested scheme. The phase can be easily detected via an interferometer, but advanced detection methods also exist [45,46]. Notably, in large neuromorphic networks, such measurements do not have to be performed after each nonlinear operation, just once at the end, where a circuit returns the result. Apart from that, in a well-tuned scheme, the output intensity level of each neuron should have the standard value ΔI, the same as that which it receives as input from other neurons. This simplifies the linking procedure between neurons and allows the construction of large-scale networks. This can always be achieved by adding an intensity rectifier at the output of a neuron. For example, such "intensity antithresholder" can be made from an additional resonator in the out-of-resonance regime with flat and horizontal $I_{\text{out}}(I_{\text{in}})$ dependence. Moreover, our results allow us to conclude that the desired output can theoretically be obtained via the same phase thresholder that we discuss here if it is properly tuned.

To explain this idea, we demonstrate the schematic dependence $I_{\text{out}}(I_{\text{in}})$ for the considered thresholder in Fig. 7(c). In the critical coupling regime, I_{out} theoretically approaches zero. However, at small deviations from the critical coupling, the minimum corresponds to a small nonzero quantity that we take as ΔI. The values of the input intensity, as discussed above, belong to some δ neighborhood of the threshold I_T. The "width" of the parabolic dependence $I_{\text{out}}(I_{\text{in}})$ is defined by the quality factor of the resonator. Notably, we can control all three parameters independently. The quantity ΔI can be varied via electrical tuning of the resonator (see below). To define δ, one may choose a desired normalization of the coupling matrix ω_{ij}, which can be divided by an arbitrary number. Finally, by choosing the right quality factor for the resonator, one can select the right level of flatness for the curve. Wider dependencies correspond to smaller qualities (because the width of the resonances increases when the quality decreases), which again appears to be an advantage of low-quality resonators in this particular case. Thus, by choosing the right values of these three parameters, one may obtain the desired value of ΔI at the output, which can be used as input for other similar neurons. The ability to realize the described mechanism experimentally depends on the characteristics of the implemented equipment, the resolution of the measurements and the manufacturing precision.

Notably, apart from being fast (theoretically terahertz scale), the nonlinear thresholder considered above is rather compact. The size of the nonlinear part presented in Fig. 7(d) is on the order of tens of microns (a resonator plus a directional coupler). MZI-based thresholders are usually much larger, on the order of hundreds of microns, since a large length is required to perform a tunable phase shift in one of their arms. The ring-resonators-based activation elements that utilize bistability effects [10] are closer to the considered micrometer length scale, but without the implementation of the low-quality factor advantages described above, they are still larger, slower, and consume more power. Even for relatively small electro-optical devices, a scaling challenge exists. The compactification and powering of large circuits is also a general challenge in the whole field of photonics at present. In the context of neuromorphic schemes, evaluations of scaling perspectives and power consumption can be found in the literature [10,43]. At present, on the basis of our theoretical investigation, it appears that the proposed device has better scaling perspectives (as a part of a neuromorphic scheme) than the existing prototypes do. For example, signal degradation is not expected to be an issue in the particular case of Fig. 7(d), since after each condition checking event in the nonlinear part of the scheme, the signal is "renewed." For the reasons discussed above (low-intensity regime), power consumption also decreases. Additionally, the electro-optical tuning mechanism discussed in detail in the next section (Sec. IV) consumes less power than the thermo-optical heaters often used in this context.

IV. ELECTRO-OPTICAL TUNING MECHANISM

As stated in the introduction, our goal is to obtain not only sharp and sensitive but also tunable thresholders with the possibility of controlling the degree of smearing of the step. Such smearing can be advantageous in certain neuromorphic algorithms [13]. Moreover, as discussed in the previous section, certain applications may require to find the right place in the vicinity of the critical coupling regime, to balance the sensitivity and transmittance. The possibility of tuning is also important in the experiment since it allows compensating for inaccuracies in the manufacturing process.

According to the results discussed in Sec. II, the balance near the critical coupling can be fulfilled via the a and b parameters in Eqs. (3) and (4) or, in other words, internal losses and coupling. The precision of the fabrication of the resonator-waveguide gap, which defines the coupling coefficient, is practically limited. However, the curvature of the activation function can be efficiently varied by introducing a well-controlled source of losses into the resonator. One of the available mechanisms known from the field of electro-optical modulation [47] can be implemented to perform tuning. Here, we demonstrate how to accomplish this via the gating of ITO. This mechanism is similar to that used in our previous works [31,34]. We use a silicon resonator similar to the one discussed above [Fig. 5(a)]. The "tuning sandwich" is placed on top of the resonator. This can be performed experimentally via thin layer deposition techniques. The sandwich includes two layers of ITO and two layers of SiO_2 [Fig. 8(a)]. Note that near the critical coupling regime, the considered effect is quite sensitive, and only a small variation in losses is needed. For this reason, the plasmonic amplification mechanisms are excessive, and metallic layers are not required inside the sandwich. The epsilon-near-zero effect, often used in this context, is also not engaged in the demonstration below.

Let us describe the tuning mechanism. The ITO/SiO_2/ITO structure works as a capacitor. When a voltage U is applied to the semiconducting layers of ITO, excessive charge can accumulate there. Thin accumulation and depletion layers with modified refractive indices are formed at the boundaries between SiO_2 and both ITO layers. The physics of this process can be described via drift-diffusion equations. The corresponding theory is described in detail in our previous works [31]. Examples of the charge density distributions inside the capacitor (along the z axis) at different voltages are shown in Fig. 8(b). With the given parameters of the capacitor (see below) and relatively small voltages (approximately 4 V), accumulation and depletion layers are formed symmetrically. At the same time, their influence on the resonator is not equivalent since one of them is closer to the disk than the other. According to our computations, the demonstrated variations are sufficient to observe the desired tuning effect.

3D modeling is required to calculate the characteristics of a resonator with an additional sandwich on top [Fig. 8(a)]. The model parameters are collected below. The waveguide cross section is 220 nm $\times$400 nm. The disk resonator radius is just 1.5 μm, which makes the considered device quite compact. The gaps between the resonator and both waveguides (which define the coupling coefficients) are 50 and 56.67 nm. The composition of the sandwich is as follows (from bottom to top): SiO_2 50 nm, ITO 50 nm, SiO_2 20 nm, and ITO 50 nm. To a large extent, the initial concentration of charge carriers in ITO (doping level) defines the original losses in the resonator before gating is applied. Using the voltages of different signs, the loss coefficient can be varied in both directions. The

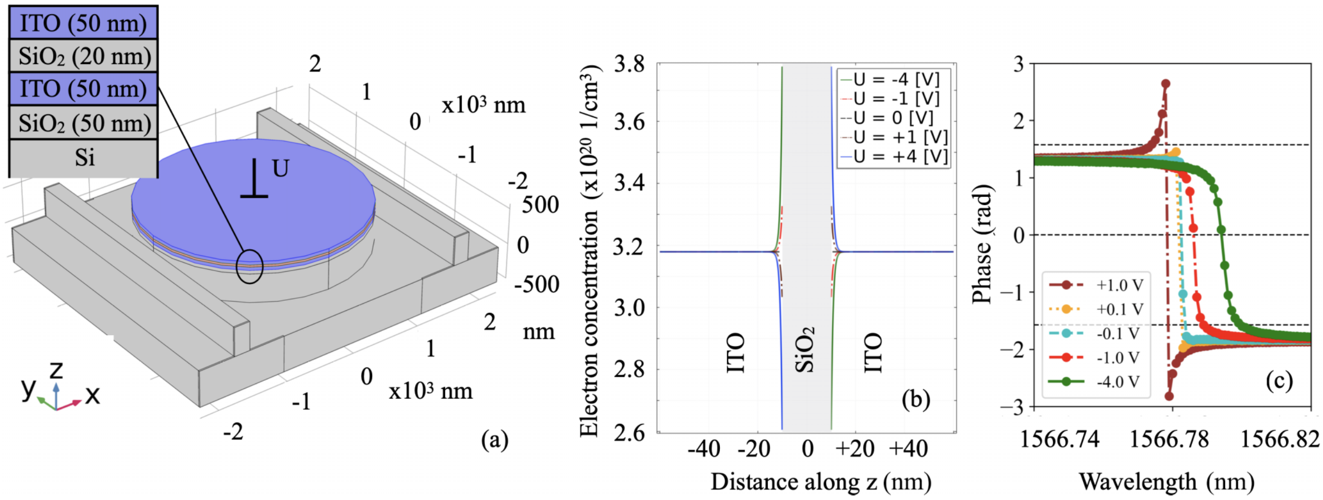

FIG. 8. Miniature disk-shaped silicon resonator with two coupled waveguides and an electro-optical tuning mechanism: (a) 3D model of the device used in the Maxwell simulations and the structure of additional active layers on top of the resonator, (b) variation in the charge distribution inside the layers of ITO at different voltages U, and (c) phase of the output signal at different voltages U. The radius of the disk is 1.5 μm, and the cross section of the waveguides is 220 nm × 400 nm. The distances between the disk and coupled waveguides are 50 and 57 nm. The thicknesses of the additional layers are shown in panel (a).

initial concentration $n_c = 3.2 \times 10^{20}$ cm^{-3} is assumed in our demonstration. This quantity can vary over a wide range of values, depending on the experimental deposition conditions. The degree of influence of the capacitor on the resonator can be varied via the width of the gap between them. The lower layer of SiO_2 is used for that purpose. In addition, the response of the capacitor to the applied voltage can be varied via the thickness of the second layer of SiO_2. It defines the distance between the capacitor plates and defines its capacitance.

The computed output phase of the device as a function of wavelength for different voltage values is shown in Fig. 8(c). At low voltages, sharp steps with a π phase shift are observed. At larger values of negative voltages, the step becomes smoother, realizing the desired type of behavior. At larger positive voltages, the step shape transforms, resulting in a 2π phase shift (which can be interpreted as the absence of a shift). This corresponds to the third scenario in Fig. 1 (green dash-dotted curve), which is not interesting for our goals. A small shift in the resonance is observed when the voltage is varied. This is a consequence of the fact that the accumulation and depletion layers vary both the imaginary and real parts of the refractive indices. In practical applications, this shift is easily compensated for by appropriately selecting values for detuning Δ. Next, any preferable nonlinear mechanism can be used to realize switching at the desired intensity I_T, as described in the previous sections. On the basis of the modeling results, the described scheme is suitable for tuning the considered phase thresholder.

V. CONCLUSION

We suggest the use of integrated optical resonators to obtain sharp intensity-dependent π phase shifts. The mechanism is based on nonlinear switching in the vicinity of the critical coupling regime. The sharpness is controllable and is not limited by the quality factors of the resonators. This effect can be utilized to construct ultrasensitive devices. Multiple advantages can be extracted from the possibility of using low-quality resonators and extremely sharp steps at the same time: compact size, low manufacturing requirements, fast switching time, low accumulated intensity and absence of overheating, and small switching intensities. The considered effect is universal and can be observed for various materials with different types of nonlinearity, including fast Kerr nonlinearity. In the latter case, the short "excitation time" of low-quality resonators can be well correlated with the typical subpicosecond time of the Kerr effect. A fast operation time can allow devices to be produced for the terahertz frequency range. The suggested thresholder may have multiple applications in optical computing. This includes logic gates and condition checking subcircuits that perform operations while keeping the incoming signals almost unperturbed. The observed behavior of the thresholder is perfect for realizing activation functions in neuromorphic chips. A photonic circuit that realizes the behavior of a single neuron on the basis of the considered thresholder is demonstrated. For the first time, to the best of our knowledge, both the phase and amplitude of light are utilized simultaneously to store and transform the state of an optical neuron. The considered neuron can act as a part of the Ising machine. The controllable smearing of the activation function, which is required by some neuromorphic algorithms, can be achieved via electrical gating of the resonator covered by suitable active materials. A numerical 3D model of the tunable resonator with a double layer of ITO is presented and discussed. The obtained characteristics are promising for successful experimental realization in the future.

ACKNOWLEDGMENTS

This work was supported by Russian Science Foundation Project No. 25-72-31023. We thank Professor N. Brilliantov, Professor I. Tyukin, and Professor E. Mirkes for fruitful discussions of neuromorphic math. We thank

Professor A. Gelash and Dr. A. Kolesnikova for the discussion of the Lugiato-Lefever model.

DATA AVAILABILITY

There are no publicly available research data or software supporting this manuscript. Requests for further information or data should be sent to the authors.

APPENDIX A: LOW-QUALITY LIMIT

An interesting question to answer is how small a quality factor could be to observe the desired sharp π phase shift. To clarify this, we return to Eq. (1). To decrease the quality factor while remaining in the critical coupling regime, one must decrease parameters a and b simultaneously, keeping their equality $a = b$. The case where $a = b = 0$ is not physically interesting since it corresponds to the situation in which all the waveguide energy is transmitted into the resonator and completely absorbed there. However, at any arbitrarily small but nonzero value of $a = b$, the considered effect takes place. We demonstrate that below.

It is known that Eq. (1) can be derived by summing the series

$$S = ib + a(1-b^2)e^{i\varphi}[1 + (iabe^{i\varphi}) + (iabe^{i\varphi})^2 + \cdots], \tag{A1}$$

where all possible tracks of light through the resonator are taken into account [4]. Assuming that $a = b$, Eq. (A1) can be considered a series in powers of a. The first term clearly does not depend on the phase, and the desired behavior should be searched starting from the second term

$$S_2 = ia + (1-a^2)ae^{i\varphi}. \tag{A2}$$

For small a, one may neglect the term $\sim a^3$ and obtain

$$S_2 \approx ia + ae^{i\varphi} = a(e^{i\pi/2} + e^{i\varphi}). \tag{A3}$$

Taking the complex argument of this function, one obtains the desired step function at $\varphi = 3\pi/2$. The function $\exp(i\varphi)$ alone does not demonstrate this type of behavior. Physically, Eq. (A3) describes the two-wave interference. The fully destructive case demonstrates the sharp phase step. To observe smearing, the amplitudes of the two terms in Eq. (A3) should be slightly different. For example, the equation

$$\Phi = \mathrm{Arg}[ia_1 + a_2e^{i\phi}] \tag{A4}$$

can be used for a simple evaluation of step broadening resulting from amplitude disbalance, taking into account that the phase φ is defined in Eq. (2) and depends on the wavelength and intensity. The number of terms in Eq. (A1) that significantly contribute to the sum decreases along with the quality factor. However, at any nonzero values of parameters $a = b$, at least two waves exist, providing the considered effect.

It can be useful in this context to analyze such a characteristic of resonators as a finesse (along with quality factors). It is defined as the free spectral range (FSR) (the distance between resonances in hertz) divided by the full width at half maximum of a resonance. Finess reflects how many iterations light passes inside a resonator. A simple analysis based on Eq. (1) allows us to derive the following analytic formula:

$$F = \left[\frac{1}{2} - \frac{1}{\pi}\arcsin\left(\frac{2a^2}{a^4+1}\right)\right]^{-1}, \tag{A5}$$

which works in the critical coupling regime. Taking the limit $a \to 0$, one obtains $F = 2$, showing that at least two terms of Eq. (A1) contribute to the sum at vanishingly small quality factors, providing the phase step. Using a similar approach, one may demonstrate that the limiting value of the quality factor at $a \to 0$ is 1.5.

Of course, the provided analysis is purely theoretical. The experimental limitations obviously prevent the $F = 2$ limit from being reached. For example, if the losses in a resonator are very high, the coupling should be accordingly large. This means that the gap between the waveguide and the resonator should be extremely small, which becomes experimentally impossible at some point. This problem can be partially solved by deforming ring resonators into oval stadiumlike shapes to increase the coupling distance. However, such solutions also have limitations. In addition, extremely large losses (small a) make it impossible to collect unused energy via the drop port, as demonstrated above. Moreover, to tune the desired curvature of the $I_{\mathrm{out}}(I_{\mathrm{in}})$ characteristics [Fig. 7(c)], multiwave interference is needed, and, correspondingly, resonators with finesses that are larger than the minimum are needed. At the same time, the effect utilized in this work is quite stable. All the regimes analyzed throughout the paper with quality factors down to $\sim$50 allow the reproduction of extremely sharp π phase steps.

APPENDIX B: NOISE ANALYSIS

To investigate the influence of noise on the suggested device and the dynamics of the pumping process, a time domain theory is needed. A direct numerical solution of time-dependent nonlinear Maxwell equations applied to resonators (even if they are low-quality resonators) is a rather slow approach. For our purposes below, we utilize the LLE, which is designed to study nonlinear phenomena in resonators, including the generation of solitons and frequency combs [48–50]. The regimes where we apply the equation are not propitious for the observation of solitons. At the same time, the usage of the theory with such a level of detalization guarantees that we do not omit any third-order nonlinear mechanism that may potentially contribute. In addition to frequency-domain Maxwell equations and the semianalytical approach based on Eqs. (3) and (4), LLE is the third computational approach used in this work to analyze the proposed effect and its applications. The self-written LLE solver realized in Fortran is used in the calculations.

One of the existing forms of the LLE equation reads [51,52]

$$\frac{d\psi}{dt} = -\left(\frac{\kappa_0 + \kappa_{\mathrm{ex}}}{2} + i\delta\omega\right)\psi + i\frac{D_2}{2}\frac{\partial^2}{\partial\theta^2}\psi + ig_0|\psi|^2\psi + I, \tag{B1}$$

where $\psi = \psi(t,\theta)$ is a dimensionless complex function, which characterizes the field amplitude (number of photons) and phase inside the resonator distributed along the angular coordinate θ. The equation contains the following parameters: κ_0 and κ_{ex}—characterize losses inside the resonator and coupling losses, respectively; $\delta\omega$—detuning; D_2—second orded disperion coefficient; g_0— nonlinear coefficient linked with material nonlinearity (Si in our case). The pumping term $I = \sqrt{\kappa_{\text{ex}} P_{\text{in}}/\hbar\omega}$ is expressed through the pump power P_{in} measured in watts. Notably, from a mathematical point of view, the LLE constitutes a damped-driven nonlinear Schrodinger equation [53–55].

To parametrize the model, we consider a small low-quality resonator characterized by the following numbers. The silicon waveguide has a cross section of 500 nm $\times$220 nm and a radius of 2 µm. This ring has a resonance at the wavelength of $\lambda_0 = 1527.06$ nm, which we consider below. The mode analysis performed in COMSOL Multiphysics allows computation of the numerical mode dispersion (effective index) $n_{\text{eff}}(\lambda)$. This dependence is used to compute the group velocity dispersion $n_g(\lambda)$ and the free spectral range:

$$n_g = n_{\text{eff}} - \lambda \frac{\partial n_{\text{eff}}}{\partial \lambda}, \tag{B2}$$

$$\text{FSR} = \frac{c}{n_g L}, \tag{B3}$$

which are used to compute the equation coefficients with the following formulas:

$$D_2 = \frac{\lambda^3 FSR^2}{c n_g} \frac{\partial^2 n_{\text{eff}}}{\partial \lambda^2}, \tag{B4}$$

$$g_0 = \frac{\hbar \omega_0^2 c n_2}{n_g^2 V_{\text{eff}}}, \tag{B5}$$

where V_{eff} is the effective volume of the mode and n_2 is the Kerr coefficient for Si. The following numbers were obtained: $n_g = 4.37$, FSR $= 5448.6$ GHz, $D_2 = -26.07$ GHz, and $g_0 = 0.011$ MHz. To ensure the critical coupling regime, two loss coefficients are equated as $\kappa_{\text{ex}} = \kappa_0 = 3.269$ THz. The quality factor is calculated from the width of the resonance obtained for this model, and its value is close to 46. The pump power P_{in} is varied between 0 and 0.7 W during the computations.

To switch from the ψ function that characterizes the state of the resonator to the transmittance measured at the output port of the coupled waveguide, the following formula, which is valid close to the center of the resonance, is applied:

$$S = \sqrt{1 - \frac{\kappa_{\text{ex}}}{\text{FSR}}} - \sqrt{1 - \frac{\kappa_0}{\text{FSR}}} \sqrt{\frac{\kappa_{\text{ex}}}{\text{FSR}}} \frac{\psi}{\psi_{\text{in}}}, \tag{B6}$$

where

$$\psi_{\text{in}} = \sqrt{\frac{P_{\text{in}}}{\hbar\omega \times \text{FSR}}}. \tag{B7}$$

Different types of noise are introduced through the last term I in Eq. (B1) as follows:

$$I = I_0[1 + A_a \sin(\omega_n t)] \tag{B8}$$

for amplitude noise and

$$I = I_0 \exp[i A_p \sin(\omega_n t)] \tag{B9}$$

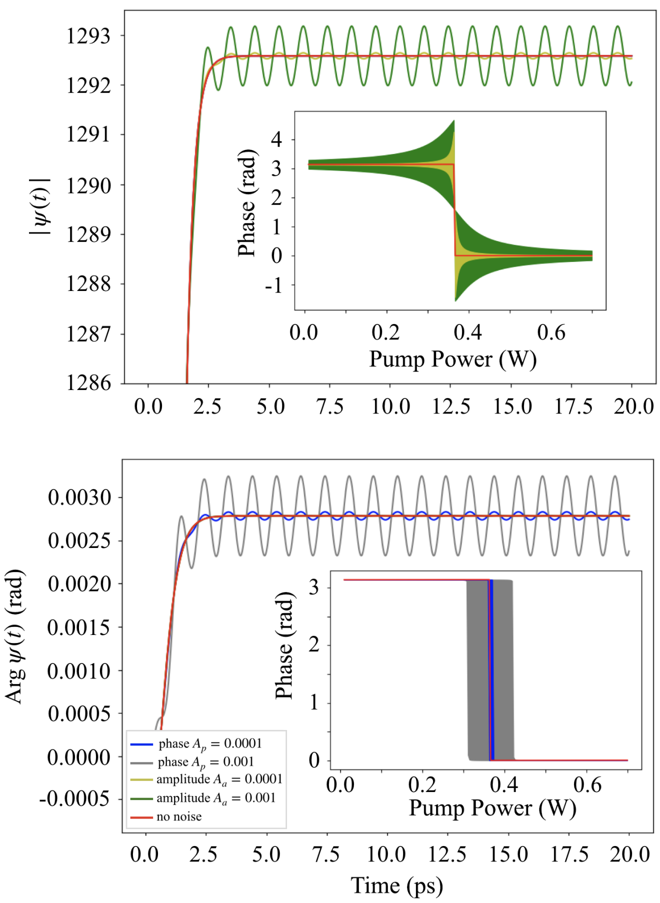

FIG. 9. The results of LLE-based time domain modeling of the thresholder. The amplitude [panel (a)] and phase [panel (b)] of the ψ function that characterizes the state of the resonator are presented as functions of time. The dynamics of the pumping process and the influence of noise are demonstrated. The insets show the influence of noise of different types on the theoretically ideal noiseless step function (red curve). Ring resonator with a radius $R = 2$ µm and loss parameters $\kappa_{\text{ex}} = \kappa_0 = 3.269$ THz (see the text) has the quality factor $Q \sim 46$.

for phase noise. Here, ω_n is the noise frequency, and A_p and A_a are the corresponding noise amplitudes.

The results of the computations are shown in Fig. 9. The time evolution of $\psi(t)$ from the initial state $\psi = 0$ under the influence of pumping is shown via red curves. Both the absolute value and the phase of ψ are shown in Figs. 9(a) and 9(b), respectively. The pumping curves reach a steady state at typical times on the order of picoseconds. This finding highlights the possibility of the considered devices operating at terahertz frequencies. The dependence of the output phase on the pump power (the step function) is shown in the insets of Fig. 9 (red curves). In the considered model of the resonator with a detuning $\delta\omega = 0.01$ THz, phase switching (appearance of the π phase step) takes place at a pump power of $\sim$0.37 W. This value is close to the value 0.75 GW/cm^2 obtained above in the paper for the different model [Fig. 5(c)] considering the waveguide cross section.

The influences of noise of different types and amplitudes on the step function are also presented in two insets in Fig. 9.

The phase noise [Eq. (B9)] with amplitudes $A_p = 0.0001$ and $A_p = 0.001$ is shown via the blue and gray curves, respectively. The amplitude noise [Eq. (B8)] with $A_a = 0.0001$ and $A_a = 0.001$ is shown via yellow and green curves, respectively. The introduction of one type of noise (amplitude or phase) causes the appearance of another type but with a much smaller amplitude. Thus, the amplitude noise (yellow and green curves) mainly contributes to the $|\psi(t)|$ [Fig. 9(a)] and is not visible in the Arg $\psi(t)$ dependence. The phase noise (blue and gray curves) is mainly visible in the Arg $\psi(t)$ dependence [Fig. 9(b)].

The frequency of noise in lasers is studied in the range of approximately 10^3–10^7 Hz [56,57]. These frequencies are significantly lower than the typical terahertz frequency of the considered thresholder. According to our numerical experiments, the noise amplitude influences the purity of the step function rather than the noise frequency. For this reason, to make the computations faster, we model the noise with the frequency $\omega_n = 2\pi \times 10^{12}$ Hz. The decrease in this value down to the range mentioned above makes the computations $\sim 10^5$ times slower, whereas the obtained results from the point of view of influence on the step function shape are analogous.

According to Fig. 9, phase noise causes "horizontal" broadening of the phase step. At the value $A_p = 0.001$ (gray curve), the thickness of the step is ~ 0.1 W. This value can be sufficient for a certain class of applications. In general, a smaller broadening is desirable and allows greater sensitivity of devices. The amplitude noise causes smearing and deformation of the step shape in the "vertical" direction. To keep the phase jump close to the desired value of π, it is preferable to have $A_a < 0.0001$, or in other words, the power fluctuations of the laser below 0.01%. However, again, the specific requirements depend on the desired application regime. Notably, even at a high level of noise, the parameters of devices can be selected such that a central (distorted) part of the step (Fig. 9 insets) is not used. The remaining part still represents a well-shaped thresholder. In summary, the presence of noise certainly decreases the theoretical "infinite sensitivity" of the considered thresholder. Thus, to make the device practical in neuromorphic applications, a certain requirement on the quality of the light source used exists. The progress in laser manufacturing and integration techniques allows positive results in the implementation of the considered devices in the future [58,59].

[1] W. Bogaerts, P. De Heyn, T. Van Vaerenbergh, K. De Vos, S. Kumar Selvaraja, T. Claes, P. Dumon, P. Bienstman, D. Van Thourhout, and R. Baets, Silicon microring resonators, Laser Photonics Rev. **6**, 47 (2012).

[2] J. Heebner, R. Grover, and T. Ibrahim, *Optical Microresonator Theory* (Springer, London, 2008).

[3] D. G. Rabus, *Integrated Ring Resonators* (Springer, Berlin, 2007).

[4] A. Yariv and P. Yeh, *Photonics: Optical Electronics in Modern Communications* (Oxford University Press, New York, 2007), Vol. 6.

[5] I. D. Rukhlenko, M. Premaratne, and G. P. Agrawal, Analytical study of optical bistability in silicon ring resonators, Opt. Lett. **35**, 55 (2010).

[6] S. Chen, L. Zhang, Y. Fei, and T. Cao, Bistability and self-pulsation phenomena in silicon microring resonators based on nonlinear optical effects, Opt. Express **20**, 7454 (2012).

[7] V. Van, T. A. Ibrahim, P. P. Absil, F. G. Johnson, R. Grover, and P.-T. Ho, Optical signal processing using nonlinear semiconductor microring resonators, IEEE J. Sel. Top. Quantum Electron. **8**, 705 (2002).

[8] C. Huang, T. F. De Lima, A. Jha, S. Abbaslou, A. N. Tait, B. J. Shastri, and P. R. Prucnal, Programmable silicon photonic optical thresholder, IEEE Photonics Technol. Lett. **31**, 1834 (2019).

[9] Q. Xu and M. Lipson, All-optical logic based on silicon microring resonators, Opt. Express **15**, 924 (2007).

[10] N. Tezak, T. Van Vaerenbergh, J. S. Pelc, G. J. Mendoza, D. Kielpinski, H. Mabuchi, and R. G. Beausoleil, Integrated coherent Ising machines based on self-phase modulation in microring resonators, IEEE J. Sel. Top. Quantum Electron. **26**, 1 (2020).

[11] N. Tezak and H. Mabuchi, A coherent perceptron for all-optical learning, EPJ Quantum Technol. **2**, 10 (2015).

[12] C. Huang, A. Jha, T. F. De Lima, A. N. Tait, B. J. Shastri, and P. R. Prucnal, On-chip programmable nonlinear optical signal processor and its applications, IEEE J. Sel. Top. Quantum Electron. **27**, 1 (2021).

[13] J. A. Hertz, *Introduction to the Theory of Neural Computation* (CRC Press, Boca Raton, FL, 2018).

[14] P. R. Prucnal and B. J. Shastri, *Neuromorphic Photonics* (CRC Press, Boca Raton, FL, 2017).

[15] W. Ertel, *Introduction to Artificial Intelligence* (Springer International Publishing AG, Switzerland, 2017).

[16] D. Kielpinski, R. Bose, J. Pelc, T. Van Vaerenbergh, G. Mendoza, N. Tezak, and R. G. Beausoleil, Information processing with large-scale optical integrated circuits, in *2016 IEEE International Conference on Rebooting Computing (ICRC)* (IEEE, New York, 2016), pp. 1–4.

[17] M. E. Newman and G. T. Barkema, *Monte Carlo Methods in Statistical Physics* (Clarendon Press, Oxford, 1999).

[18] J. R. R. Campo and D. Pérez-López, Reconfigurable activation functions in integrated optical neural networks, IEEE J. Sel. Top. Quantum Electron. **28**, 1 (2022).

[19] A. Ghosh, A. Pal, S. Zhang, L. Hill, T. Bi, and P. Del'Haye, Phase symmetry breaking of counterpropagating light in microresonators for switches and logic gates, Laser Photonics Rev. **20**, e01500 (2026).

[20] I. A. Pshenichnyuk, F. Yousry, D. S. Zemtsov, S. S. Kosolobov, and V. P. Drachev, Nonlinear optical switching in hybrid plasmonic waveguides, Phys. Rev. B **109**, 035401 (2024).

[21] J. E. Heebner, V. Wong, A. Schweinsberg, R. W. Boyd, and D. J. Jackson, Optical transmission characteristics of fiber ring resonators, IEEE J. Quantum Electron. **40**, 726 (2004).

[22] F. Liu, T. Wang, L. Qiang, T. Ye, Z. Zhang, M. Qiu, and Y. Su, Compact optical temporal differentiator based on silicon microring resonator, Opt. Express **16**, 15880 (2008).

[23] M. Chalupnik, A. Singh, J. Leatham, M. Lončar, and M. Soltani, Scalable and ultralow power silicon photonic two-dimensional phased array, APL Photonics **8**, 051305 (2023).

[24] M. Burla, B. Crockett, L. Chrostowski, and J. Azaña, Ultra-high Q multimode waveguide ring resonators for microwave photonics signal processing, in *2015 International Topical Meeting on Microwave Photonics (MWP)* (IEEE, New York, 2015), pp. 1–4.
[25] H. A. Haus, *Waves and Fields in Optoelectronics* (Prentice-Hall, Inc., NJ, USA, 1984).
[26] R. Boyd, *Nonlinear Optics* (Elsevier, Amsterdam, 2020).
[27] C. Valagiannopoulos and V. Kovanis, Nonlinear resonances in fast electronic circuits mimicking photonic oscillators, Chaos, Solitons Fractals **157**, 111912 (2022).
[28] C. Valagiannopoulos, Multistability in coupled nonlinear metasurfaces, IEEE Trans. Antennas Propag. **70**, 5534 (2022).
[29] A. Armaroli, P. Feron, and Y. Dumeige, Stable integrated hyperparametric oscillator based on coupled optical microcavities, Opt. Lett. **40**, 5622 (2015).
[30] N. Jebali, L. Bodiou, J. Charrier, A. Armaroli, and Y. Dumeige, Combining FDTD and coupled-mode theory for self-pulsing modeling in coupled nonlinear microring resonators, J. Opt. Soc. Am. B **37**, 2557 (2020).
[31] I. A. Pshenichnyuk, G. I. Nazarikov, S. S. Kosolobov, A. I. Maimistov, and V. P. Drachev, Edge-plasmon assisted electro-optical modulator, Phys. Rev. B **100**, 195434 (2019).
[32] I. A. Pshenichnyuk, S. S. Kosolobov, and V. P. Drachev, Towards deep integration of electronics and photonics, Appl. Sci. **9**, 4834 (2019).
[33] I. A. Pshenichnyuk, S. S. Kosolobov, and V. P. Drachev, Fine-tuning of the electro-optical switching behavior in indium tin oxide, Phys. Rev. B **103**, 115404 (2021).
[34] D. S. Zemtsov, I. A. Pshenichnyuk, S. S. Kosolobov, A. K. Zemtsova, D. M. Zhigunov, A. S. Smirnov, K. N. Garbuzov, and V. P. Drachev, Plasmon-assisted Si-ITO integrated electro-optical rib-shape modulator, J. Lightwave Technol. **41**, 6310 (2023).
[35] M. Borghi, D. Bazzanella, M. Mancinelli, and L. Pavesi, On the modeling of thermal and free carrier nonlinearities in silicon-on-insulator microring resonators, Opt. Express **29**, 4363 (2021).
[36] A. Jha, C. Huang, and P. R. Prucnal, Reconfigurable all-optical nonlinear activation functions for neuromorphic photonics, Opt. Lett. **45**, 4819 (2020).
[37] R. Dekker, A. Driessen, T. Wahlbrink, C. Moormann, J. Niehusmann, and M. Först, Ultrafast Kerr-induced all-optical wavelength conversion in silicon waveguides using 1.55 μm femtosecond pulses, Opt. Express **14**, 8336 (2006).
[38] N. Vukovic, N. Healy, F. Suhailin, P. Mehta, T. Day, J. Badding, and A. Peacock, Ultrafast optical control using the Kerr nonlinearity in hydrogenated amorphous silicon microcylindrical resonators, Sci. Rep. **3**, 2885 (2013).
[39] Y. Kim and S.-H. Hong, Inverse design of compact silicon photonic waveguide reflectors and their application for Fabry–Perot resonators, Nanophotonics **13**, 2829 (2024).
[40] M. W. Pruessner, T. H. Stievater, and W. S. Rabinovich, Integrated waveguide Fabry-Perot microcavities with silicon/air Bragg mirrors, Opt. Lett. **32**, 533 (2007).
[41] F. Ashtiani, A. J. Geers, and F. Aflatouni, An on-chip photonic deep neural network for image classification, Nature (London) **606**, 501 (2022).
[42] M. M. P. Fard, I. A. D. Williamson, M. Edwards, K. Liu, S. Pai, B. Bartlett, M. Minkov, T. W. Hughes, S. Fan, and T.-A. Nguyen, Experimental realization of arbitrary activation functions for optical neural networks, Opt. Express **28**, 12138 (2020).
[43] Y. Shen, N. C. Harris, S. Skirlo, M. Prabhu, T. Baehr-Jones, M. Hochberg, X. Sun, S. Zhao, H. Larochelle, D. Englund, *et al.*, Deep learning with coherent nanophotonic circuits, Nat. Photonics **11**, 441 (2017).
[44] N. C. Harris, J. Carolan, D. Bunandar, M. Prabhu, M. Hochberg, T. Baehr-Jones, M. L. Fanto, A. M. Smith, C. C. Tison, P. M. Alsing, *et al.*, Linear programmable nanophotonic processors, Optica **5**, 1623 (2018).
[45] M. Song, J. Steinmetz, Y. Zhang, J. Nauriyal, K. Lyons, A. N. Jordan, and J. Cardenas, Enhanced on-chip phase measurement by inverse weak value amplification, Nat. Commun. **12**, 6247 (2021).
[46] J. Milvich, D. Kohler, W. Freude, and C. Koos, Integrated phase-sensitive photonic sensors: A system design tutorial, Adv. Opt. Photonics **13**, 584 (2021).
[47] K. Liu, C. R. Ye, S. Khan, and V. J. Sorger, Review and perspective on ultrafast wavelength-size electro-optic modulators, Laser Photonics Rev **9**, 172 (2015).
[48] L. A. Lugiato and R. Lefever, Spatial dissipative structures in passive optical systems, Phys. Rev. Lett. **58**, 2209 (1987).
[49] T. Kippenberg, A. Gaeta, M. Lipson, and M. Gorodetsky, Dissipative Kerr solitons in optical microresonators, Science **361**, eaan8083 (2018).
[50] X. Ji, X. Li, Z. Qiu, R. N. Wang, M. Divall, A. Gelash, G. Lihachev, and T. J. Kippenberg, Deterministic soliton microcombs in Cu-free photonic integrated circuits, Nature (London) **646**, 843 (2025).
[51] L. Lugiato, F. Prati, and M. Brambilla, *Nonlinear Optical Systems* (Cambridge University Press, Cambridge, 2015).
[52] D. Pidgayko, A. Tusnin, J. Riemensberger, A. Stroganov, A. Tikan, and T. J. Kippenberg, Voltage-tunable optical parametric oscillator with an alternating dispersion dimer integrated on a chip, Optica **10**, 1582 (2023).
[53] I. Barashenkov and Y. S. Smirnov, Existence and stability chart for the AC-driven, damped nonlinear Schrödinger solitons, Phys. Rev. E **54**, 5707 (1996).
[54] I. A. Pshenichnyuk and N. G. Berloff, Inelastic scattering of xenon atoms by quantized vortices in superfluids, Phys. Rev. B **94**, 184505 (2016).
[55] I. Pshenichnyuk, Static and dynamic properties of heavily doped quantum vortices, New J. Phys. **19**, 105007 (2017).
[56] W. Jin, Q.-F. Yang, L. Chang, B. Shen, H. Wang, M. A. Leal, L. Wu, M. Gao, A. Feshali, M. Paniccia, *et al.*, Hertz-linewidth semiconductor lasers using CMOS-ready ultra-high-Q microresonators, Nat. Photonics **15**, 346 (2021).
[57] G. Lihachev, J. Riemensberger, W. Weng, J. Liu, H. Tian, A. Siddharth, V. Snigirev, V. Shadymov, A. Voloshin, R. N. Wang, *et al.*, Low-noise frequency-agile photonic integrated lasers for coherent ranging, Nat. Commun. **13**, 3522 (2022).
[58] C. Xiang, W. Jin, O. Terra, B. Dong, H. Wang, L. Wu, J. Guo, T. J. Morin, E. Hughes, J. Peters, *et al.*, 3D integration enables ultralow-noise isolator-free lasers in silicon photonics, Nature (London) **620**, 78 (2023).
[59] P. A. Morton and M. J. Morton, High-power, ultra-low noise hybrid lasers for microwave photonics and optical sensing, J. Lightwave Technol. **36**, 5048 (2018).